RSC Advances

PAPER

View Article Online
View Journal | View Issue

Cite this: *RSC Adv.*, 2025, **15**, 43763

Photodetector based on bis-2,6-[2-(2-oxoindolin-3-ylidene)malononitrile]naphthalene derivatives/zinc oxide nanorod heterostructures with machine vision observation and artificial intelligence pattern recognition

Cheng-Shan Chen,[a] Yi-Hao Cai,[b] Yu-Hong Yang,[b] Zong-Liang Huang,[b] Hao-Zhu Zhang,[b] YewChung Sermon Wu, *[a] Ming-Hsien Li, *[c] Ming-Yu Kuo,*[d] Hsiang Chen *[b] and Yung-Hui Li [e]

Zinc oxide (ZnO)-based photodetectors have made significant progress in the field of broadband photodetection in recent years due to their ease of integration with low-bandgap semiconductors. Although the intrinsic bandgap of 3.2 eV for pure ZnO limits its response to wavelengths outside the ultraviolet (UV) light region, researchers have successfully extended its detection range into the visible light region through material modifications and heterojunction designs. This study investigates the use of the bis-2,6-[2-(2-oxoindolin-3-ylidene)malononitrile]naphthalene derivative (teven-518)/ZnO nanocomposite as a photodetector. The molecular structure of teven-518 possesses a high electron affinity that is further enhanced by the strong electron-withdrawing nature of the malononitrile groups, which improves electron transport capability. Additionally, the introduction of the naphthalene unit enhances molecular coplanarity, resulting in a rigid and planar structure that promotes π–π stacking between molecules, thereby improving the charge carrier mobility. On the other hand, the C2C6 side chains in the molecule provide moderate intermolecular interactions, enabling uniform film formation during solution processing. Through the integration of code development and model training, along with material characterization and photodetection results, this study confirms that the addition of teven-518 with ZnO nanorods contributes to the enhancement of ZnO-based photodetector performance, showing significant improvements in both machine learning-based recognition and model evaluation.

Received 7th July 2025
Accepted 21st October 2025

DOI: 10.1039/d5ra04832j

rsc.li/rsc-advances

1 Introduction

In the continuously advancing field of optoelectronic devices, the pursuit of high-performance and multifunctional photodetectors (PDs) remains a key driving force behind technological innovation. Metal oxides, such as zinc oxide (ZnO),[1] and compound semiconductors, such as gallium nitride (GaN),[2] are promising materials for photodetection applications. In recent years, wide-bandgap GaN has attracted significant attention due to its high electron mobility, excellent thermal stability, and strong resistance to high-energy radiation and chemical corrosion.[3] However, the fabrication of GaN nanostructures requires high-temperature processes and chemical etching, which not only consume a large amount of energy but also increase the production cost of GaN-based devices. Therefore, the pursuit of high-performance PDs with low energy consumption is critical.

ZnO has emerged as a potential material for cost-effective and high-performance PDs due to its low-temperature processing (≤100 °C), high thermal stability, and excellent electronic properties.[4] However, its wide band gap of 3.2 eV limits its photoresponse to ultraviolet (UV) light. Integrating organic compounds with ZnO-based PDs is a promising strategy to achieve wideband photodetection while maintaining low-energy consumption, owing to the ease of integration and low-temperature processing. Various organic compounds, such as poly(3,4-ethylenedioxythiophene):poly(styrenesulfonate) (PEDOT:PSS),[5] *N*,*N*′-dioctyl-3,4,9,10-perylenedicarboximide (PDIC8),[6] and bisindolo quinoxaline-tips (BIQ-TIPs),[7] have been shown to significantly enhance the spectral response of ZnO-based photodetectors.

[a]*Department of Materials Science and Engineering, National Yang Ming Chiao Tung University, Taiwan. E-mail: sermonwu@nycu.edu.tw*

[b]*Department of Applied Materials and Optoelectronic Engineering, National Chi Nan University, Taiwan. E-mail: hchen@ncnu.edu.tw*

[c]*Department of Electro-Optical Engineering, National Formosa University, Taiwan. E-mail: mhli1125@nfu.edu.tw*

[d]*Department of Applied Chemistry, National Chi Nan University, Taiwan. E-mail: mykuo@ncnu.edu.tw*

[e]*AI Research Center, Hon Hai Research Institute, No. 32 Jihu Rd., Neihu District, Taipei, 114699, Taiwan*

Bis-2,6-[2-(2-oxoindolin-3-ylidene) malononitrile] naphthalene derivatives (teven-518) are n-type organic semiconductor materials with a highly conjugated structure. Their molecular design incorporates oxoindoline, malononitrile, and naphthalene groups, providing excellent optical and electrical properties. The deep lowest unoccupied molecular orbital (LUMO) levels of teven-518 can be attributed to the enhanced electron-withdrawing behavior of its side chain, which promotes air stability when applied in optoelectronic devices.[8] Due to its good air stability, outstanding electron transport capability, and tunable photoelectric response characteristics,[9] this material shows great potential in optoelectronic applications. The molecule exhibits high electron affinity, and the strong electron-withdrawing characteristics of the malononitrile group[10,11] resulting in a LUMO energy level of approximately −3.96 eV, which is compatible with the conduction band minimum (CBM) of ZnO, enhancing electron transport efficiency. Additionally, the introduction of naphthalene units enhances the coplanarity of the molecule,[12] resulting in a rigid planar structure that facilitates π–π stacking between molecules, improving charge carrier mobility.[13–15] The indoline group, modified through oxidation, enhances the molecule's electron-accepting characteristics, providing excellent electron transfer capabilities.[16,17] On the other hand, the C2C6 side chains within the molecule provide moderate intermolecular interactions, enabling the formation of uniform films during solution processing. Moreover, teven-518 exhibits a broad UV-visible absorption range (∼300–650 nm), making it suitable for various optoelectronic applications.

In this study, the organic material of teven-518 was deposited onto the surface of ZnO nanorods (NRs) *via* spin-coating for the application of broadband photodetection PDs. In terms of optical absorption, teven-518 covers the ultraviolet to visible light range (∼300–650 nm) and possesses a high absorption coefficient, making it an ideal candidate for use in light-sensing applications. Through various material characterization analyses, it was confirmed that the organic compound teven-518 was successfully deposited on ZnO NRs *via* spin-coating. Sensing analysis results showed that the performance of this sensor in light detection surpassed that of pure ZnO PDs, with a significantly enhanced photoresponse in the visible light wavelength range. For machine learning and model recognition, a code was developed to read six time series datasets. These datasets correspond to devices exposed to consecutive on/off light illumination cycles from six different light sources. Each time series was segmented into fixed-length segments and assigned a class label. The dataset was then divided into training and test sets, and a one-dimensional convolutional neural network (1D CNN) model was trained on this data. Finally, the model's performance was evaluated on both the training and test sets, including the calculation of accuracy and the generation of a confusion matrix.

2 Experiment

2.1. ZnO NR growth

To fabricate the ZnO NRs sensing layer, a seed solution was first prepared by dissolving zinc acetate in ethanol with the addition of a small amount of monoethanolamine (MEA) as a stabilizing agent. The solution was heated in a water bath at 60 °C under continuous magnetic stirring at 80 rpm for 30 minutes to ensure complete dissolution and homogenization. The resulting precursor solution was stored for 24 hours at room temperature to obtain a clear and stable seed solution suitable for spin coating. Prior to the deposition of the ZnO seed layer, the substrates, which were already deposited with an interdigitated gold electrode, were thoroughly cleaned using the RCA method. The seed layer was deposited *via* a two-step spin-coating process: initially at 500 rpm for 5 seconds, followed by 3000 rpm for 30 seconds. After coating, the substrates were dried on a hotplate at 130 °C. This spin-coating and drying cycle was repeated five times to ensure uniform seed layer formation. Subsequently, the seeded substrates were immersed in a ZnO NRs growth solution containing equimolar concentrations of zinc nitrate and hexamethylenetetramine (HMTA) dissolved in deionized water. The hydrothermal growth process was carried out in a preheated water bath maintained at 70 °C for 1 hour to facilitate the vertical growth of ZnO NRs.[18] Following growth, the substrates were thoroughly rinsed with deionized water and subjected to thermal annealing in a furnace at 300 °C for 1 hour to enhance crystallinity and ensure the structural integrity of the ZnO NRs layer.

2.2. Measurement

For the photosensing experimental setup, an Agilent 4155C semiconductor parameter analyzer was used to bring the probe into contact with the electrodes of the devices. The dark current (I_D) of the devices was measured under dark conditions (*i.e.*, without illumination). Subsequently, a light source was activated, and the illuminated current (I_P) was measured. By calculating the I_P/I_D ratio, we were able to quantify the current increase under illumination relative to the dark current, thereby evaluating the device's sensing performance under light exposure.[19] Following this, current–voltage (*I–V*) characteristic measurements were performed to gain deeper insight into the current response of the devices under various applied voltages. At the same time, we recorded the photocurrent–time (*I–t*), which reflects the temporal response of the devices to the switching of the light source. This allowed us to assess the sensitivity and response speed of the devices under illumination with different light sources.

Photoresponse measurements were carried out under six light sources with different wavelengths: ultraviolet light-emitting diode (LED) (UV LED, peak wavelength = 380 nm), white LED (W LED), blue LED (B LED, peak wavelength = 442 nm), green LED (G LED, peak wavelength = 530 nm), red LED (R LED, peak wavelength = 654 nm), and infrared LED (IR LED, peak wavelength = 850 nm). By plotting the *I–t* response curves, we were able to compare the sensing performances of different devices under various light wavelengths and further investigate the correlation between the optoelectronic properties and the wavelength of incident light. After completing the *I–t* measurements, the instrument was switched back to *I–V* measurement mode. Under illumination, the Agilent 4155C

instrument was used to measure the photocurrent of devices biased within a voltage range of −5 V to +5 V. This process enabled us to obtain more precise data on the device's photoelectric response under different voltage conditions.

2.3. Machine learning and model recognition

In this study, six time-series datasets of *I*–*t* responses were first extracted from an Excel file. These datasets were captured from devices exposed to consecutive on/off light illumination cycles from six different light sources, including infrared, red, green, blue, white, and UV LEDs. To ensure consistency, all sequences were transformed and organized into a matrix form, converting column vectors into row vectors. The sampling rate was 0.75 points per second, and the single *I*–*t* curve waveform had a total duration of 60 seconds, consisting of 30 seconds with the light source on, followed by 30 seconds with the light source off.

The original *I*–*t* waveforms, each consisting of 80 data points (corresponding to 60 seconds at a sampling rate of 0.75 points per second), were segmented using a sliding-window approach. A frame shift of 25 data points was used, meaning that the window advanced by 25 points for each extracted segment. Each resulting segment contained 25 data points, corresponding to a temporal duration of 18.75 seconds (25×0.75 s). Given a total length of 80 data points per waveform and a stride of 25, the overlap ratio between adjacent segments was calculated as $1 - (25/80) = 0.69$, indicating that approximately 69% of the data points were shared between neighboring segments.

For model training, the segmented data were further processed to generate input sequences of 750 sampling points per segment, using an appropriate framing strategy. Class labels were assigned based on the corresponding illumination conditions. To avoid data leakage, segmentation was performed after grouping the original sequences according to the device and illumination source. The dataset was then partitioned into training, validation, and test sets in a 70%, 15%, and 15% ratio, respectively, with only the validation set used for hyperparameter tuning. The final input tensor fed into the 1D CNN was structured as [batch size, length, channels] = [25, 750, 1], where each mini-batch contained 25 single-channel sequences of length 750.

For model construction, a 1D CNN was employed for feature extraction and classification. The architecture consisted of three convolutional layers with 10, 15, and 15 filters, and kernel sizes of 15, 10, and 5, respectively. Each convolutional layer was followed by a ReLU activation function and batch normalization. A flattened layer was applied after the final convolutional block to convert the feature maps into a one-dimensional vector. As the number of filters and kernel sizes were moderate, the parameter count remained manageable even after flattening. A fully connected layer and a softmax output layer were used for final classification.

The model was implemented using the MATLAB Deep Learning Toolbox and trained using the Stochastic Gradient Descent with Momentum (SGDM) optimizer, with an initial learning rate of 1×10^{-4}. No learning rate decay schedule or weight decay was applied. The training was conducted with a mini-batch size of 25 for a maximum of 100 epochs. Early stopping was not applied; instead, training was allowed to proceed for the full number of epochs. The final model was selected based on training progress and final validation accuracy. All input data were standardized using *Z*-score normalization, applied individually to each time series to eliminate scale differences across sequences.

For model evaluation, in addition to the confusion matrix and accuracy, precision, recall, and F_1-scores were reported to provide a more comprehensive performance assessment. Given the slight class imbalance, weighted F_1-score and balanced accuracy were also included. Furthermore, Grad-CAM was employed for model interpretability analysis, revealing that the CNN was particularly sensitive to the rising edges and steady-state regions of the time-series signals. This observation was consistent with the experimental results, thereby validating the rationality and potential applicability of the model.[20]

The code flow shown in Scheme 1 is as follows: six sets of time-series data of *I*–*t* curves are first loaded, followed by handling missing values (NaN) and segmenting the data. Corresponding labels are then generated, and the data are normalized. After preprocessing, the dataset is divided into training and test sets. A 1D CNN model is then defined and trained. Finally, the model's accuracy is evaluated on both the

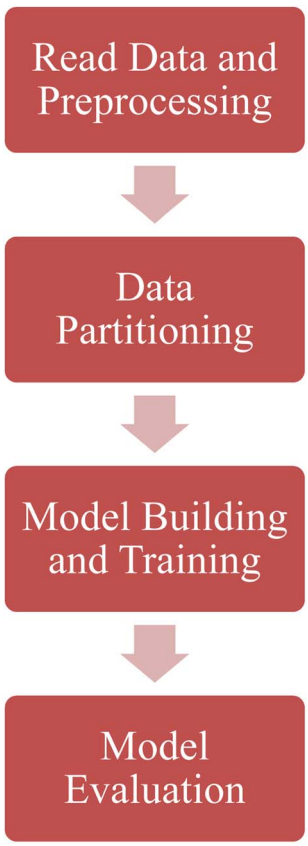

Scheme 1 The practical operational steps of the CNN model are outlined for the classification of *I*–*t* curves from the ZnO-based and ZnO/teven-518-based PDs under different light sources.

training and test sets, and the classification results are visualized using a confusion matrix.

3 Results and discussion

Fig. 1(a) displays an optical microscope (OM) image of teven-518 deposited on the ZnO NRs, labeled as ZnO/teven-518, at 400× magnification. The surface appears uniformly green, with red regions indicating elevated areas. Fig. 1(b) presents an OM image at a higher magnification (1000×), revealing more microscopic details. The particle distribution appears relatively uniform, though some localized aggregation is still observed. Macroscopical surface roughness analysis results are shown in Fig. 1(c) and (d). Fig. 1(c) presents the three-dimensional (3D) topography of the ZnO/teven-518 surface, with a measured maximum height of approximately 31.0 μm. The surface appears relatively uniform, though areas with higher particle elevations (red regions) and lower flat regions (green regions) are still visible. Fig. 1(d) provides a higher-resolution image of the ZnO/teven-518 surface structure, with a measured maximum height of approximately 6.7 μm, revealing smaller-scale surface undulations. Compared to the 400× image, this higher-magnification image shows more fine microscopic particles, indicating that teven-518 is non-uniformly coated on the ZnO NRs' surface.

Scanning electron microscopy (SEM) was employed to analyze the surface morphology of the ZnO/teven-518 sample. Fig. 2(a) presents a top-view SEM image, revealing the uneven coverage of teven-518 over the ZnO NRs. Additionally, the image confirms that the ZnO NRs exhibit a vertically aligned, clustered growth morphology. As shown in Fig. 2(b), SEM combined with energy-dispersive X-ray spectroscopy (EDS) confirmed the presence of carbon, oxygen, silicon, and zinc elements, indicating the successful deposition of the organic layer teven-518 on the ZnO NRs.

Fig. 2(c) shows a transmission electron microscope (TEM) image of the cross-sectional structure of the ZnO/teven-518 nanocomposite. The ZnO NRs are clearly visible, with teven-518 covering their surfaces, forming well-defined heterostructures.[21,22] The ZnO NRs are arranged in an orderly fashion, indicating a uniform growth process, which plays a crucial role in enhancing the response of the photodetector. In terms of photosensing, the well-aligned ZnO NRs contribute to improved light absorption efficiency, and the ZnO/teven-518 heterojunction enhances the separation of photogenerated electron–hole pairs.

Fig. 2(d) shows a magnified view of the interface between the ZnO NRs and teven-518. The internal structure of the ZnO NRs and the coating of teven-518 can be clearly observed. The lattice structure visible within some of the ZnO NRs indicates that they

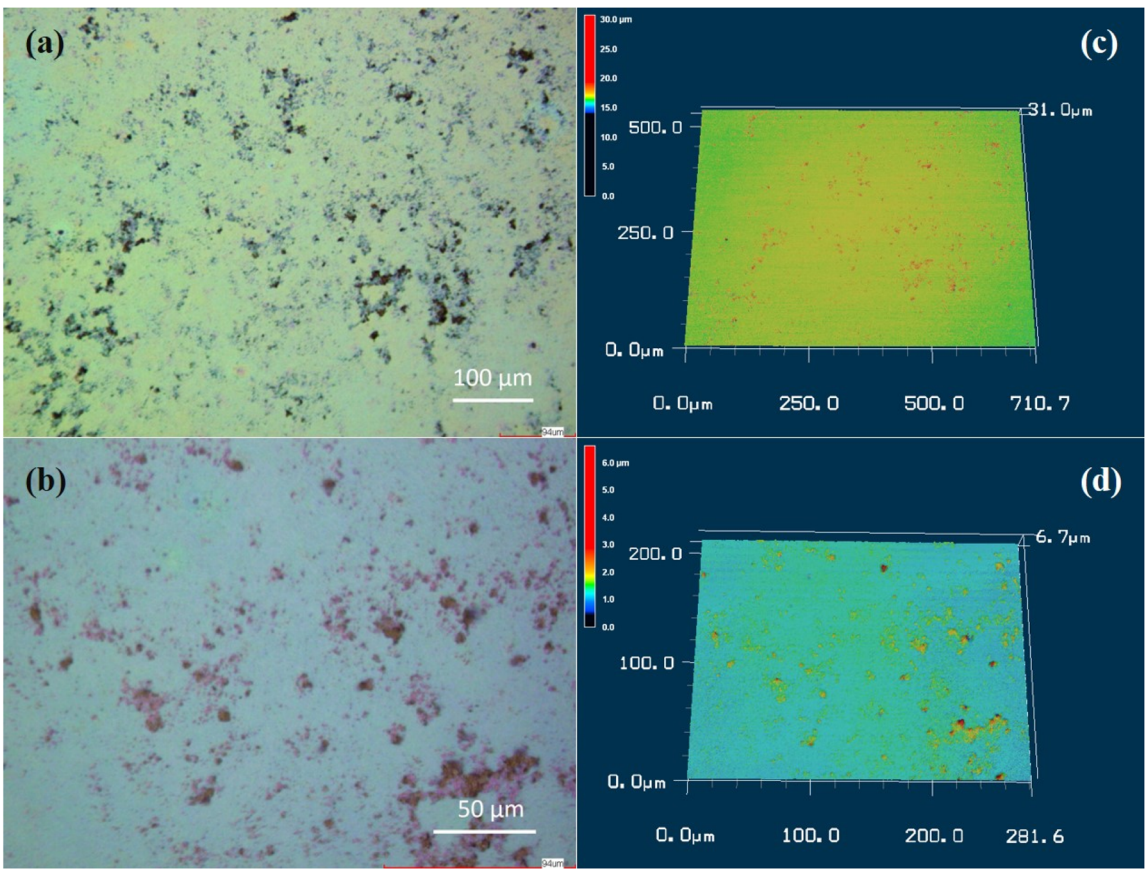

Fig. 1 OM images of teven-518 deposited on the ZnO NRs with (a) low magnification (400×) and (b) high magnification (1000×). 3D OM images of teven-518 deposited on the ZnO NRs with (c) low and (d) high magnification.

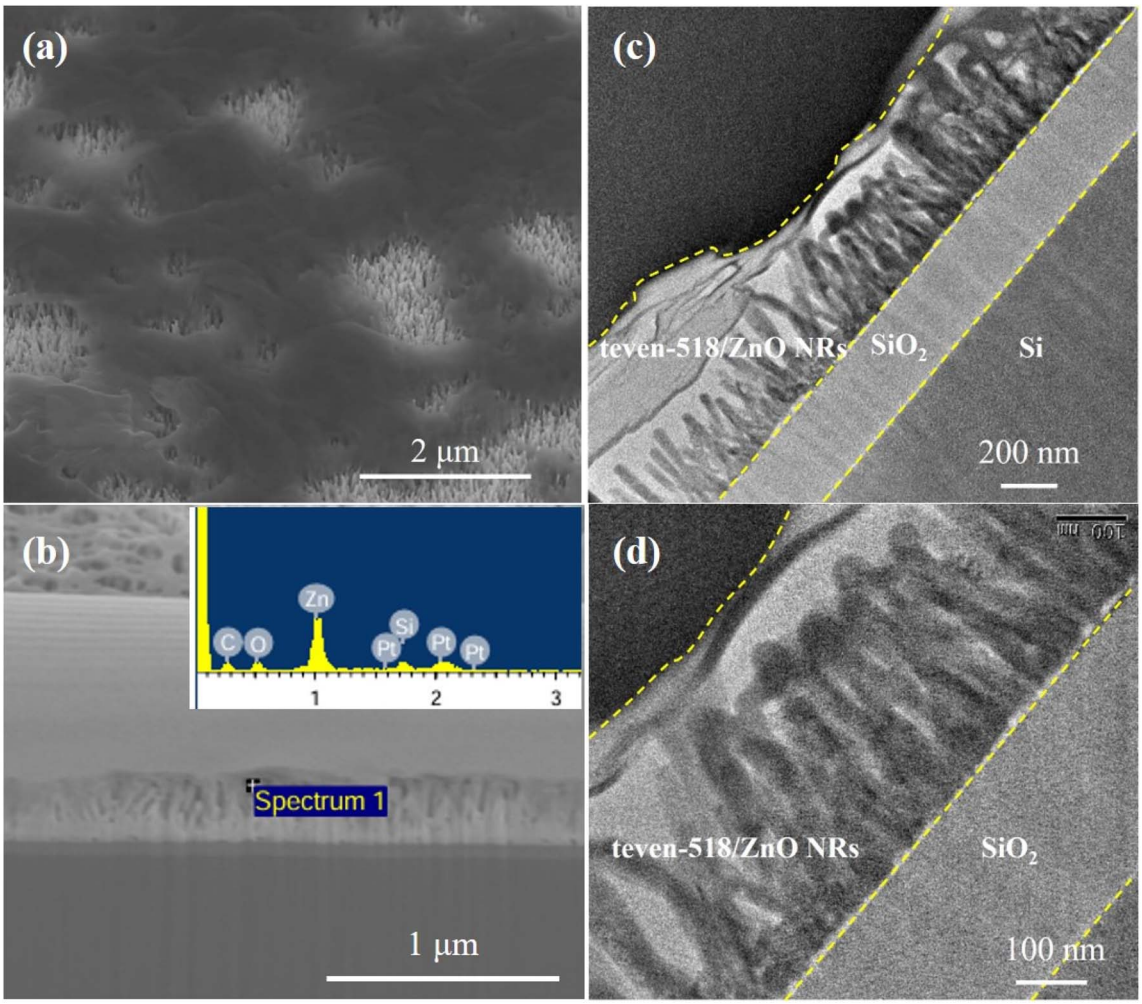

Fig. 2 (a) Top-view and (b) cross-sectional SEM image of teven-518 deposited on the ZnO NRs. The inset in (b) reveals the EDX spectrum at the marked position. TEM image of the ZnO/teven-518 sample with (c) low and (d) high magnification.

retain a high degree of crystallinity. High crystallinity in ZnO NRs ensures the efficient transport of photogenerated electrons, reducing the recombination between electrons and holes, and thereby enhancing the photoelectric conversion efficiency. Furthermore, teven-518 is closely contacted with the ZnO NRs, forming an electron pathway for charge carrier transport from teven-518 to ZnO NRs.

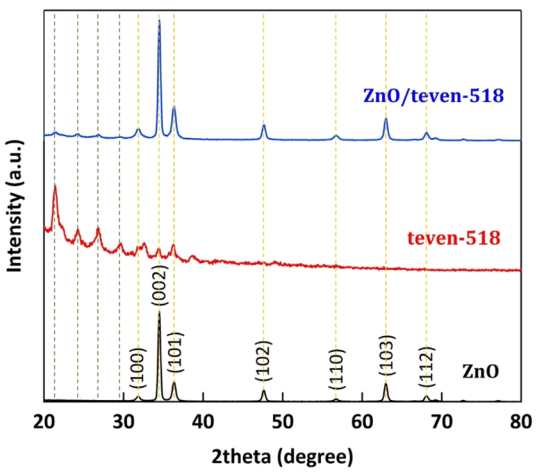

Fig. 3 XRD profiles of the ZnO NRs, teven-518, and ZnO/teven-518 samples.

Fig. 3 presents the X-ray diffraction (XRD) profiles of the ZnO NRs, teven-518, and ZnO/teven-518 samples. The ZnO NRs sample exhibits a prominent XRD peak at 2θ of approximately 34.5°, corresponding to the (002) facet of the hexagonal ZnO NRs. After covering the ZnO NRs with teven-518, the XRD profiles show that the characteristic XRD peaks of ZnO remain present. Additional XRD peaks at lower 2θ are assigned to crystalline teven-518, as compared to the XRD profile of teven-518. These XRD peaks are presumably ascribed to the self-assembly of teven-518.

As shown in Fig. 4(a), the UV-Vis absorption spectrum of the ZnO/teven-518 heterostructure reveals a cut-off absorption wavelength at 712 nm. This absorption edge is significantly red-shifted compared to that of pure ZnO NRs, which is observed at 393.2 nm. The red shift indicates that the formation of the heterostructure effectively extends the material's absorption range, particularly into the visible light region. This absorption

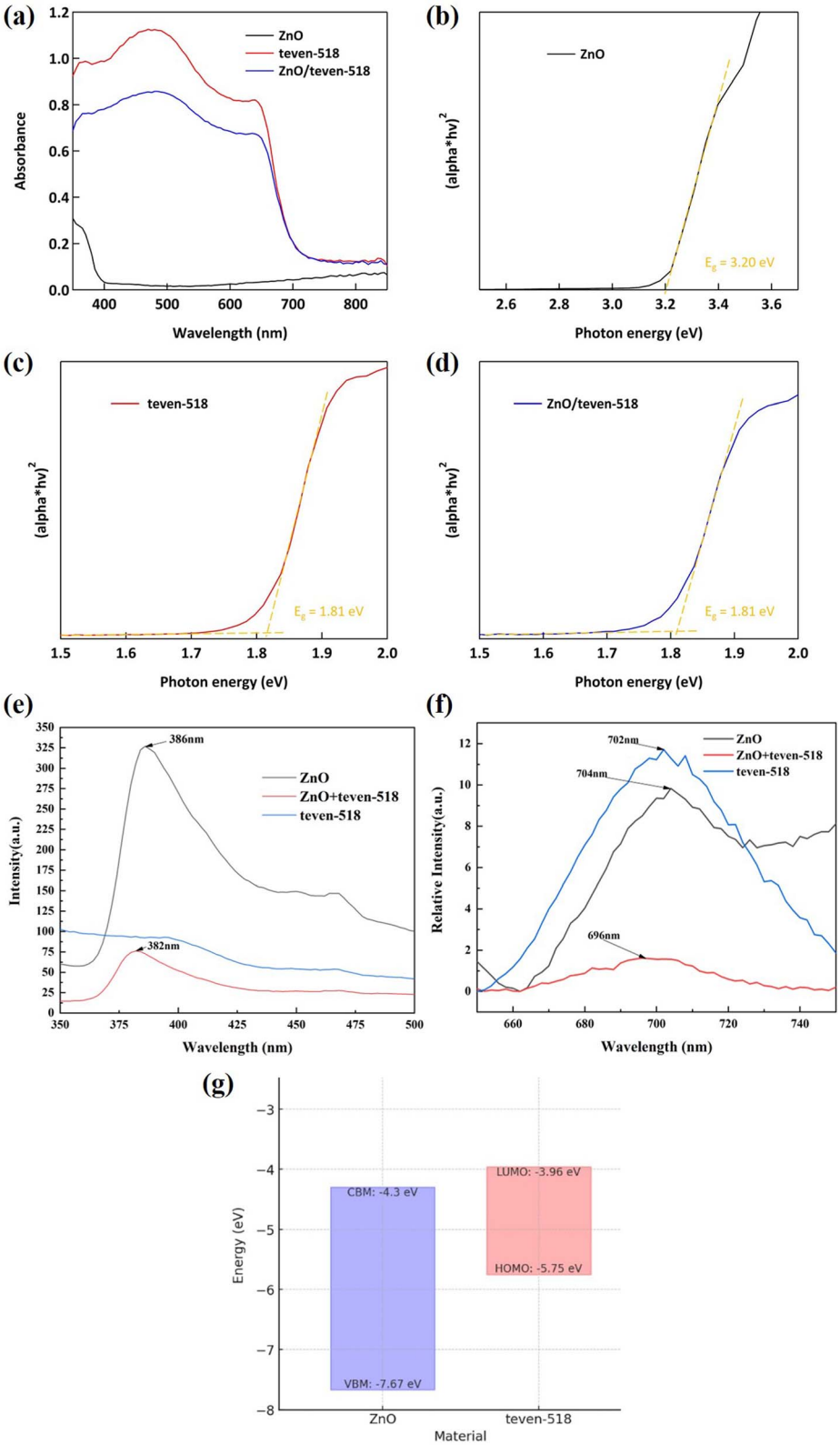

Fig. 4 (a) UV-Vis absorption spectra of the ZnO NRs, teven-518, and ZnO/teven-518 samples. Tauc plots of the (b) ZnO NRs, (c) organic teven-518, and (d) ZnO/teven-518 grown on a slide substrate. (e) PL emission spectra of the ZnO, teven-518, and ZnO/teven-518 samples excited with a 325 nm laser. (f) Energy band diagram of the ZnO/teven-518 heterostructure.

edge can be used to estimate the optical bandgap (E_g) of the ZnO/teven-518 heterostructure. As shown in Fig. 4(b)–(d), the calculated bandgap for ZnO/teven-518 is approximately 1.81 eV, which is notably lower than that of pure ZnO (3.20 eV) and consistent with that of teven-518 (1.81 eV). This result suggests that the ZnO/teven-518 heterostructure possesses enhanced visible-light absorption capabilities, making it a promising candidate for optoelectronic applications under solar or ambient light conditions.

As shown in Fig. 4(e), the photoluminescence (PL) spectrum of ZnO NRs in the ultraviolet region exhibits a strong near-band-edge (NBE) emission peak at 386 nm, characteristic of its direct bandgap emission. The peak intensity and position of this NBE emission indicate that the ZnO NRs possess good crystallinity with relatively low defect density. However, in the ZnO/teven-518 heterostructure, the main emission peak blue-shifts to 382 nm. This shift is attributed to the modulation of surface states by the teven-518 molecules, which reduces the surface defect density and leads to a localized increase in the bandgap. In contrast, no significant PL signal is observed for the teven-518 material alone in this region, indicating that teven-518 primarily acts as a surface modifier rather than an active light-emitting component in the heterostructure.

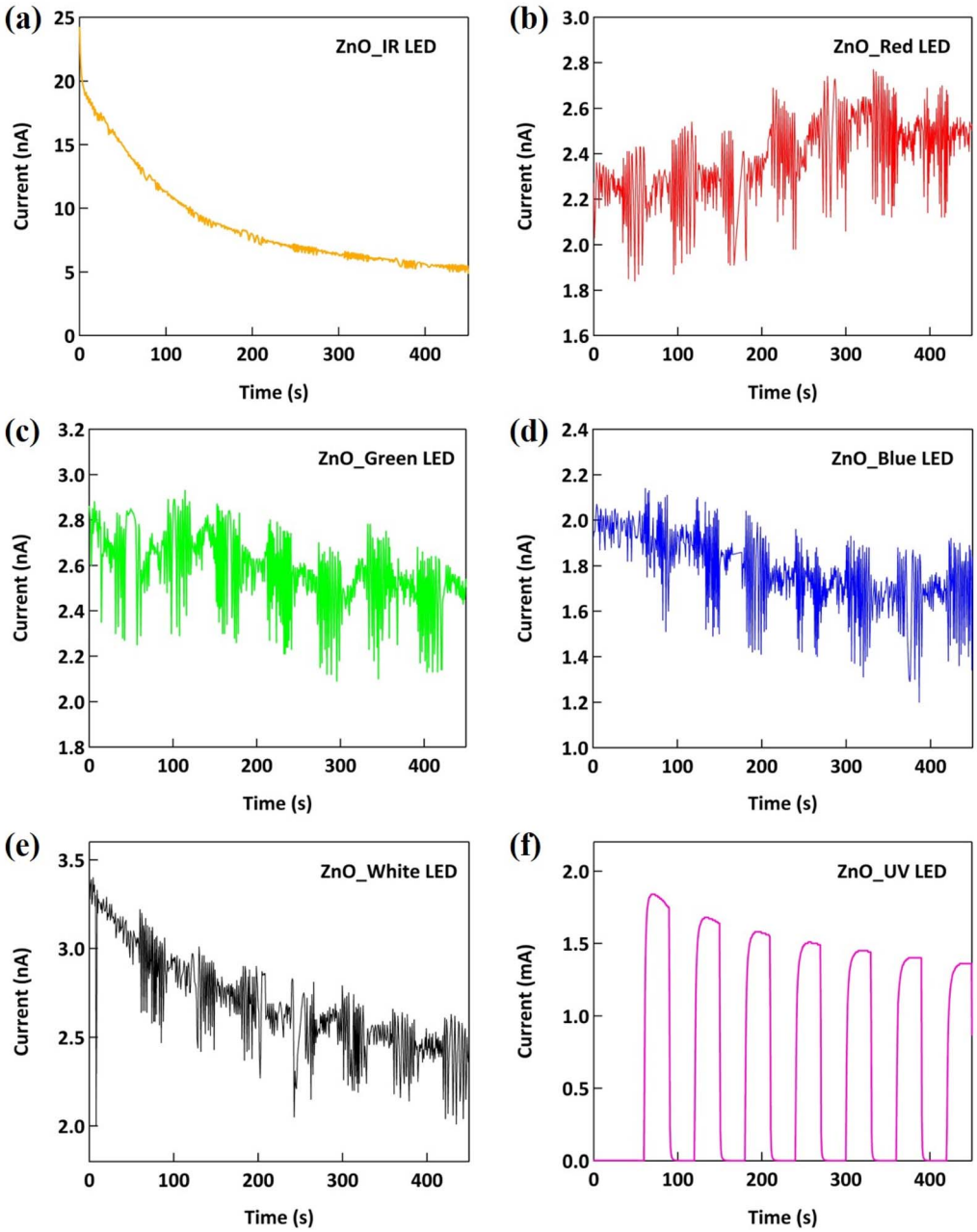

Fig. 5 I–t curves of the ZnO device under the consecutive on/off light illumination of (a) IR LED, (b) red LED, (c) green LED, (d) blue LED, (e) white LED and (f) UV LED.

The deep-level emission (DLE) of ZnO NRs at 524 nm is another prominent feature in its PL spectrum and is closely associated with defect states such as oxygen vacancies (V_O). This defect-related emission reflects the distribution of intrinsic and surface defects within the ZnO material.[23] In comparison, the emission intensity in this region is significantly reduced in the ZnO/teven-518 heterostructure, indicating that the teven-518 modification effectively suppresses defect-state-related luminescence in ZnO. This suppression can be attributed to the formation of an organic overlayer by teven-518 molecules on the ZnO surface, which passivates existing surface defect states. Furthermore, the incorporation of teven-518 enhances the separation efficiency of photogenerated electron–hole pairs at the ZnO/teven-518 interface, thereby further diminishing the radiative recombination associated with deep-level defects.

The emission in the red-light region is concentrated between 696–704 nm and primarily originates from radiative recombination associated with deep-level defect states, as seen in Fig.

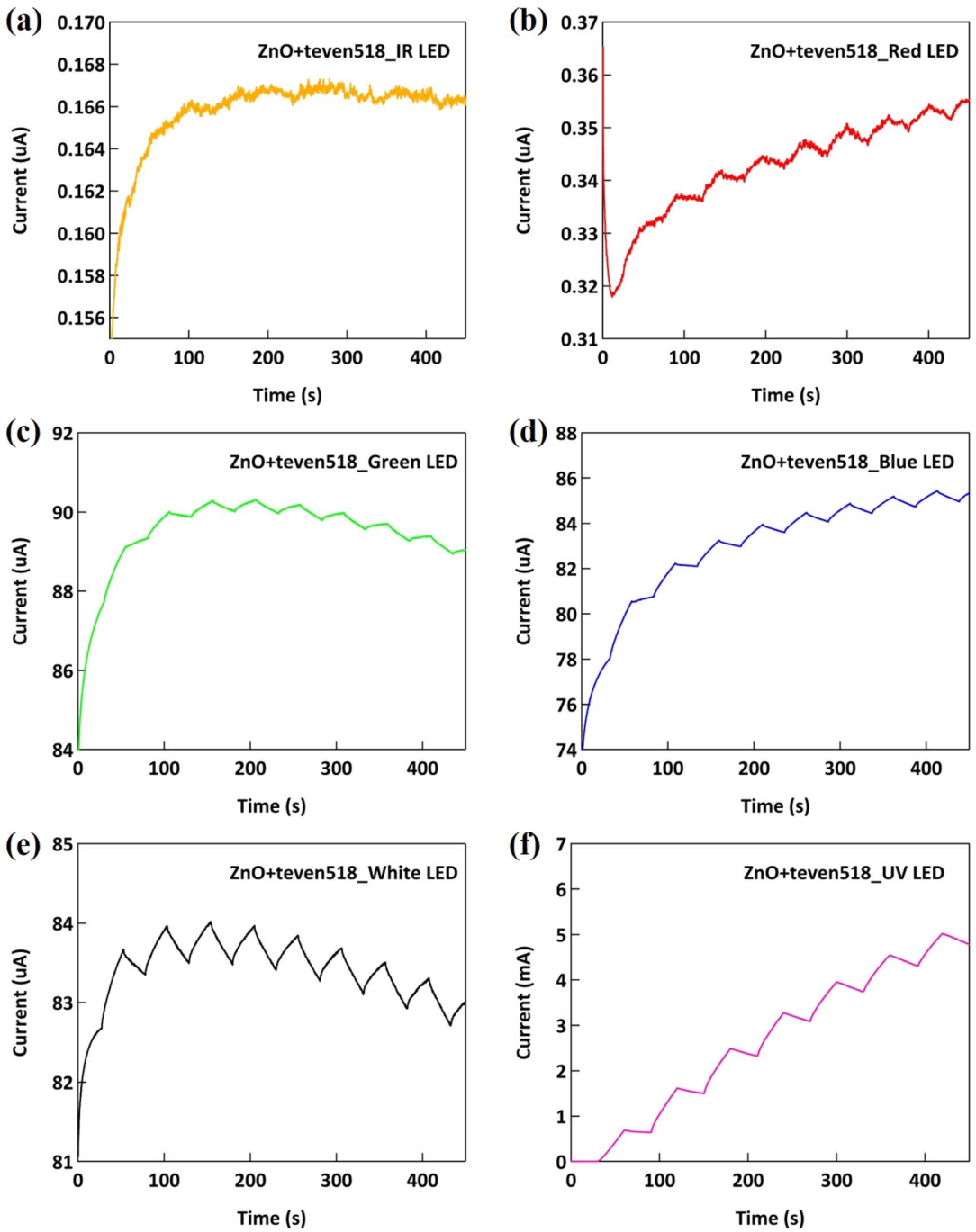

Fig. 6 *I*–*t* curves of the ZnO/teven-518 device under the consecutive on/off light illumination of (a) IR LED, (b) red LED, (c) green LED, (d) blue LED, (e) white LED and (f) UV LED.

4f. In the PL spectrum of pure ZnO NRs, a prominent emission peak appears at 704 nm, indicating a high activity of deep-level defects. In contrast, for the ZnO/teven-518 heterostructure, the emission peak is blue-shifted to 696 nm, and its intensity is significantly reduced, suggesting that the teven-518 modification effectively passivates the deep-level defects in ZnO NRs. Additionally, the teven-518 material itself exhibits a red emission peak at 702 nm, indicating that teven-518 inherently possesses strong red-light emission properties. This emission is attributed to specific luminescent functional groups within the teven-518 molecular structure, which complement the red emission characteristics of ZnO in this spectral region.

The mechanism of optical sensing mainly comes from the combined effect of electron–hole pairs generated by photoexcitation, which react with the oxygen ions adsorbed on the surface of ZnO NRs, leading to the reduction of depletion regions. When photogenerated electrons migrate through the conduction band of ZnO NRs, they can flow through an external circuit, resulting in a measurable photocurrent. ZnO has a bandgap of 3.20 eV, while the organic material teven-518 has a bandgap of 1.81 eV. Fig. 4(g) shows the energy band alignment of the ZnO/teven-518 heterostructure. When irradiated with light, teven-518 can absorb visible and ultraviolet light to generate electron–hole pairs, and the heterostructure of ZnO/teven-518 forms an appropriate band step at the interface, so that photogenerated electrons mainly accumulate in the conduction band of ZnO NRs, and the photogenerated holes migrate to the valence band of teven-518, so that the signal generated by the light can be effectively detected.

Pure ZnO NRs are a typical wide-bandgap semiconductor material with an energy gap of about 3.20 eV, corresponding to the abruption in the ultraviolet region (wavelength less than 370 nm). In ZnO NRs with intact structures and low defect density, the electronic energy state is concentrated within the valence band and the conduction band, and there is no intermediate energy level or trap state in the bandgap, so its light response is mainly limited to the ultraviolet band. However, for long-wavelength light sources with low energy, *i.e.*, visible light such as blue, green, and red, the photon energy is not strong enough to overcome the bandgap of ZnO to effectively excite

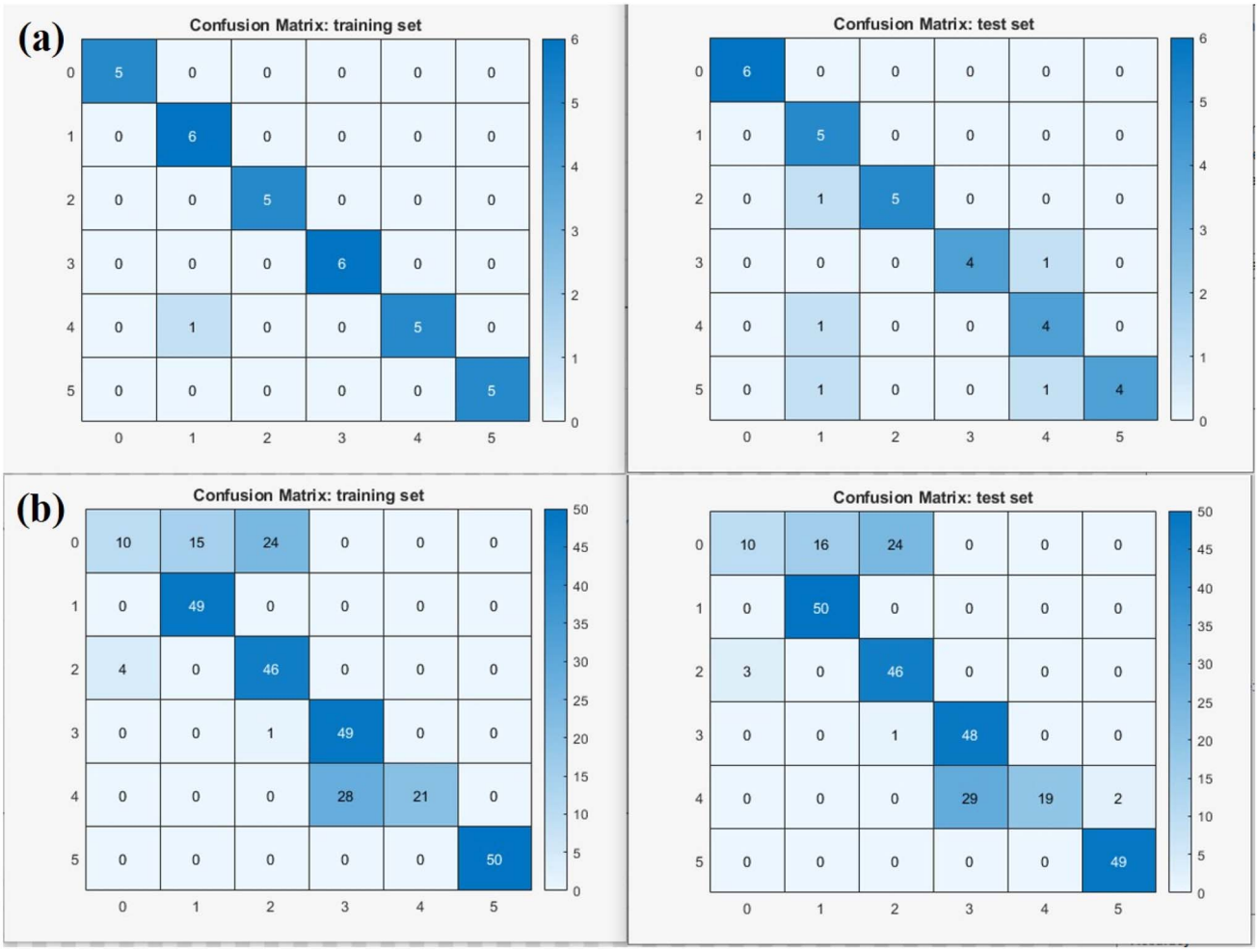

Fig. 7 Machine identification analysis diagram for the (a) ZnO-based and (b) ZnO/teven-518-based devices under the consecutive on/off light illumination from six different sources. The light sources are labelled as follows: white LED (0), green LED (1), blue LED (2), infrared LED (3), red LED (4), and UV LED (5).

electron–hole pairs, so there is almost no photocurrent response, as shown in Fig. 5.

In contrast, the ZnO/teven-518 heterostructure device exhibits obvious photocurrent response under red, blue, green, and white LEDs illumination, as shown in Fig. 6. The results show that the PD based on the ZnO/teven-518 heterostructure has successfully extended its light response range to the visible region. This improvement can be attributed to the fact that teven-518 absorbs visible light and generates electron–hole pairs, which can be efficiently injected into the conduction band of ZnO NRs, where photocurrent is formed through the external circuitry. These results show that the modification of the organic material teven-518 can effectively improve the sensing ability of ZnO NRs devices for visible light, demonstrating the potential of this heterostructure in the development of full-spectrum optical sensors.

Through model simulation and learning, we have integrated the photodetection measurements of ZnO NRs-based PDs combined with teven-518 under six different light sources into a 1D CNN model. The data processing flow chart is shown in Scheme 1. First, the time-series *I*–*t* data were segmented into fixed-length intervals, with each segment labelled according to its corresponding class. The dataset was then divided into training and testing sets, and the CNN model was trained using these photodetection signals. After evaluating the model's performance on both the training and testing data, a confusion matrix was generated to calculate the classification accuracy. In the confusion matrix, labels 0 to 5 correspond to the devices under consecutive on/off light illumination from six different sources: white LED (0), green LED (1), blue LED (2), infrared LED (3), red LED (4), and UV LED (5), respectively. The results shown in Fig. 7 reveal that the model can clearly distinguish between different light sources. In particular, the ZnO NRs-based PDs exhibited a strong concentration along the diagonal of the confusion matrix, indicating high classification accuracy; a similar trend was observed when combined with the organic compound teven-518. Furthermore, the time-domain features learned by the CNN model were highly consistent with the actual measurement results, further validating the effectiveness and reliability of the photodetection system.

4 Conclusions

We have developed a ZnO NRs/teven-518 heterojunction-based light sensor with significantly improved photocurrent response, carrier separation, and transport efficiency compared to pure ZnO sensors. The sensor showed fast response, high stability, and long-term reliability, with photoluminescence confirming reduced carrier recombination. Additionally, a 1D CNN was applied to time-series data from photocurrent responses, achieving high classification performance with precision, recall, and F_1-scores. Grad-CAM analysis revealed the model's sensitivity to key signal features, aligning with experimental results. This work highlights the potential of organic–inorganic composites in optical sensing and paves the way for future intelligent sensing technologies.

Author contributions

The manuscript was written through contributions of all the authors. All the authors have approved the final version of the manuscript. Cheng-Shan Chen: data curation, formal analysis, and writing – original draft; Yi-Hao Cai: data curation, formal analysis, investigation, methodology, and writing – original draft; YewChung Sermon Wu: supervision, resources, funding acquisition and writing – review & editing; Ming-Hsien Li: formal analysis, funding acquisition, writing – original draft, and writing – review & editing; Ming-Yu Kuo: formal analysis, methodology, supervision, writing – original draft, and writing – review & editing; Hsiang Chen: conceptualization, formal analysis, funding acquisition, methodology, supervision, writing – original draft, and writing – review & editing; Yung-Hui Li: resources; and Jung Han: resources.

Conflicts of interest

There are no conflicts to declare.

Data availability

The data that support the findings of this study are available from the corresponding author upon reasonable request.

Acknowledgements

The authors are grateful for research grants from the National Science and Technology Council (NSTC 113-2112-M-150-002, NSTC 114-2112-M-150-002, NSTC 113-2221-E-260-005). This work is also supported by NSTC T-Star Center Project: Future Semiconductor Technology Research Center under NSTC 114-2634-F-A49-001.

References

1 K. M. Wasman and B. Hamadameen, Review of optoelectronic properties of ZnO photodetector, *J. Phys. Chem. Funct. Mater.*, 2022, **5**(1), 9–21.
2 N. K. R. Nallabala, *et al.*, High performance, self-powered and thermally stable 200–750 nm spectral responsive gallium nitride (GaN) based broadband photodetectors, *Sol. Energy Mater. Sol. Cells*, 2021, **225**, 111033.
3 Y. Peng, *et al.*, Improvement of GaN-Based Device Performance by Plasma-Enhanced Chemical Vapor Deposition (PECVD) Directly Preparing h-BN with Excellent Thermal Management Characteristics, *Molecules*, 2025, **30**(6), 1307.
4 J. Ding, *et al.*, Ultraviolet photodetectors based on wide bandgap semiconductor: a review, *Applied Physics A*, 2024, **130**(5), 350.
5 K. Arjun and B. Karthikeyan, Flexible ultraviolet photodetector based on flower-like ZnO/PEDOT: PSS nanocomposites, *Applied Physics A*, 2022, **128**(5), 449.
6 Y.-Y. Tsai, M.-H. Li and M.-Y. Kuo, Material analysis and broadband photoresponse characteristics of ZnO/N, N'-

Dioctyl-3, 4, 9, 10-perylenedicarboximide (PDI-C8) composite materials with organic nanostructures deposited on ZnO nanorods, *Results Phys.*, 2025, **70**, 108180.

7 Y.-S. Tsai, *et al.*, Incorporation of hydrophobic-like bisindolo quinoxaline-tips (BIQ-TIPs) aggregation on ZnO nanorods for spectral broadening photodetection, *Results Phys.*, 2022, **34**, 105318.

8 A. P. Dhondge, *et al.*, Angular-shaped naphthalene Bis (1, 5-diamide-2, 6-diylidene) malononitrile for high-performance, air-stable n-type organic field-effect transistors, *Org. Lett.*, 2018, **20**(9), 2538–2542.

9 S. Ren, *Synthesis of novel π-conjugated functional organic semiconductors for optoelectronic applications*, Institut Polytechnique de Paris, 2021.

10 M. Yang, *et al.*, Near-infrared electron acceptors with cyano-substituted 2-(3-Oxo-2, 3-dihydroinden-1-ylidene) malononitrile end-groups for organic solar cells, *ACS Energy Lett.*, 2023, **8**(6), 2641–2651.

11 R. Gokul, *et al.*, Exploring the potential of malononitrile functionalized donor–acceptor systems for non-volatile memory device applications, *Phys. Chem. Chem. Phys.*, 2025, **27**(1), 129–137.

12 M. Xu, *et al.*, Coplanar Conformational Structure of π-Conjugated Polymers for Optoelectronic Applications, *Adv. Mater.*, 2024, **36**(1), 2301671.

13 Y. Chen, *et al.*, Semiconducting Copolymers with Naphthalene Imide/Amide π-Conjugated Units: Synthesis, Crystallography, and Systematic Structure-Property-Mobility Correlations, *Angew. Chem.*, 2022, **134**(39), e202208201.

14 T. Mikie, *et al.*, Naphthobispyrazine bisimide: a strong acceptor unit for conjugated polymers enabling highly coplanar backbone, short π–π stacking, and high electron transport, *Chem. Mater.*, 2022, **34**(6), 2717–2729.

15 L. Jing, *et al.*, Influence of π–π interactions on organic photocatalytic materials and their performance, *Chem. Soc. Rev.*, 2025, **54**(4), 2054–2090.

16 S. S. Malhotra, *et al.*, Exploring the effect of aromatic π-spacers on the photophysical properties of triphenylamine and indoline dyes in DSSCs, *Opt. Quantum Electron.*, 2025, **57**(1), 1–27.

17 Z. Abid, *et al.*, Quinoxaline derivatives as attractive electron-transporting materials, *Beilstein J. Org. Chem.*, 2023, **19**(1), 1694–1712.

18 S. Baruah and J. Dutta, Hydrothermal growth of ZnO nanostructures, *Sci. Technol. Adv. Mater.*, 2009, **10**(1), 013001.

19 S.-L. Gao, *et al.*, Persistent photoconductivity of metal oxide semiconductors, *ACS Appl. Electron. Mater.*, 2024, **6**(3), 1542–1561.

20 C.-H. Lee, *et al.*, Interface-tailored ZnO/BDPQ-Oct inorganic/organic dual sensors for improved light/gas detection and artificial intelligence-enabled gas recognition, *J. Mater. Chem. C*, 2025, **13**(30), 15310–15321.

21 K. Ganjehyan, *et al.*, P-type π-conjugated BTPDS-8 organic molecule for broadband hybrid photodetector with organic/inorganic heterostructure, *Sens. Actuators, A*, 2024, **367**, 115048.

22 A. K. Dwivedi, S. Jit and S. Tripathi, High-responsivity PEDOT: PSS/SnS 2/MoS 2 double-heterostructure-based organic–inorganic broadband photodetector, *IEEE Trans. Electron Devices*, 2023, **70**(9), 4694–4699.

23 H. Shen, *et al.*, Defects control and origins of blue and green emissions in sol-gel ZnO thin films, *Vacuum*, 2022, **202**, 111201.